

1      **Protein-Based Enzyme Bionanoreactor for Efficient**  
2      **CO<sub>2</sub> Mineralization under Benign Conditions**

3

4                  *Yifei Ma<sup>a</sup>, Meng Wang<sup>a,\*</sup>*

5

6       <sup>a</sup>Department of Civil and Environmental Engineering, University of Pittsburgh, 3700 O'Hara St.,  
7       Pittsburgh, PA 15261, USA

8       \*Address correspondence to [meng.wang@pitt.edu](mailto:meng.wang@pitt.edu), 412-624-9207

9

10     **Keywords**

11     protein nanocage, encapsulation, carbon capture and sequestration, biomineralization, air capture

12

13     **Conflict of Interest**

14     The authors declare no conflict of interest.

15      **Abstract**

16           Mineralization is an emerging approach for carbon capture and sequestration (CCS), but current  
17          methods rely on high pH conditions to overcome the kinetic and thermodynamic barriers of CO<sub>2</sub> reacting  
18          with metal cations to form carbonate minerals. This is often achieved through adding alkaline chemicals or  
19          using electrochemical catalysis, which are resource-intensive, environmentally disruptive, and require  
20          extensive pH adjustments. Inspired by natural biomineralization, this study presents a novel enzyme  
21          bionanoreactor approach based on self-assembling lumazine synthase AaLS-13 protein nanocages to  
22          facilitate efficient CO<sub>2</sub> mineralization under mild conditions. The AaLS-13 nanocage actively encapsulates  
23          and concentrates metal cations within its cavity, with its assembled structure playing a critical role in  
24          enhancing the cation availability for subsequent reactions. By encapsulating carbonic anhydrase into the  
25          nanocages, the resultant bionanoreactors integrate CA catalysis with metal cation concentration, showing  
26          significantly improved catalytic performance. They efficiently convert dissolved CO<sub>2</sub> into carbonate  
27          minerals as well as capture and mineralize atmospheric CO<sub>2</sub> under benign, ambient conditions. This  
28          research lays the groundwork for developing AaLS-13 nanocage-based bionanoreactors for sustainable  
29          carbon mineralization, offering an eco-friendly CCS alternative. It also provides new insights into  
30          leveraging AaLS-13 nanocage-substrate interactions to modulate local microenvironments and optimize  
31          enzyme catalysis for diverse nanotechnological, biomedical, and environmental applications.

32     **1. Introduction**

33         The rising levels of atmospheric carbon dioxide ( $\text{CO}_2$ ) are a major driver of global climate change,  
34         prompting urgent efforts to develop effective carbon capture and sequestration (CCS) solutions.<sup>[1]</sup> Among  
35         them, mineralization, which converts  $\text{CO}_2$  to stable, solid carbonate minerals, is gaining increased attention  
36         for its ability to provide permanent carbon storage.<sup>[2,3,4]</sup> This approach involves reacting dissolved  $\text{CO}_2$  with  
37         mineral cations like magnesium ( $\text{Mg}^{2+}$ ) and calcium ( $\text{Ca}^{2+}$ ) to form carbonate minerals.<sup>[5,6]</sup> These cations  
38         can be obtained from various sources such as mining effluent, paper recycling wastewater, and hydraulic  
39         fracturing wastewater.<sup>[7,8]</sup> Seawater presents another promising source, containing approximately 10 mM  
40          $\text{Ca}^{2+}$  and 40 mM  $\text{Mg}^{2+}$ .<sup>[9]</sup> With its vast volume, seawater-based mineralization offers a potential pathway  
41         for gigatonne-scale  $\text{CO}_2$  management.<sup>[10]</sup> However, the hydration of dissolved  $\text{CO}_2$  ( $\text{CO}_2 + \text{H}_2\text{O} \rightarrow \text{H}_2\text{CO}_3$ )  
42         is exceedingly slow, with a second-order reaction rate constant of  $6 \times 10^{-4} \text{ M}^{-1} \text{ s}^{-1}$  at neutral pH, which  
43         represents a major bottleneck in the carbon mineralization process by limiting the availability of carbonate  
44         species.<sup>[11]</sup> In addition, at benign pH, the large majority of carbonate species remain in the form of  
45         bicarbonate ( $\text{HCO}_3^-$ ), resulting in a low concentration of carbonate ions ( $\text{CO}_3^{2-}$ ) and further impeding the  
46         formation of carbonate minerals. To overcome these limitations, current carbon mineralization systems  
47         often use high pH conditions (>10), by either adding alkaline chemicals directly or generating hydroxide  
48         ions in situ through electrochemical catalysis.<sup>[12,13]</sup> While these methods accelerate  $\text{CO}_2$  hydration and  
49         increase  $\text{CO}_3^{2-}$  concentration, they are chemical- or energy-intensive, require pH readjustments, and can  
50         disrupt aquatic ecosystems, which pose significant drawbacks for economic viability, large-scale  
51         applications, and long-term sustainability.<sup>[14,15,16]</sup>

52         The mineralization of  $\text{CO}_2$  is indeed a common process in the biosphere, known as carbon  
53         biomineralization, where living organisms convert  $\text{CO}_2$  into solid carbonate minerals and deposit them  
54         within biological structures such as shells and exoskeletons.<sup>[17]</sup> Biochemical studies have identified a variety  
55         of biomolecules – including enzymes, proteins, polysaccharides, and lipids – that play crucial roles in  
56         facilitating carbon biomineralization.<sup>[2,18,19]</sup> These biomolecules contribute synergistically in two main  
57         ways: by catalyzing the hydration of  $\text{CO}_2$  and by concentrating mineral cations, thus enabling the efficient

58 precipitation of carbonate minerals even under benign ambient conditions. One of the key players is  
59 carbonic anhydrase (CA), a group of metalloenzymes that catalyze the interconversion between dissolved  
60 CO<sub>2</sub> and bicarbonate.<sup>[20,21]</sup> As one of the most efficient enzymes known, CA accelerates the CO<sub>2</sub>-water  
61 reaction with a rate constant of 10<sup>6</sup> M<sup>-1</sup> s<sup>-1</sup> at neutral pH, approximately 10<sup>9</sup> faster than the uncatalyzed  
62 reaction.<sup>[22]</sup> This high catalytic activity makes CA broadly used in carbon biomineralization to bypass the  
63 rate-limiting CO<sub>2</sub> hydration step. In addition to CA, biomolecules with abundant acidic functional groups  
64 (e.g., carboxyl groups) play a vital role in concentrating metal cations through electrostatic  
65 interactions.<sup>[23,24,25]</sup> They create localized microenvironments with significantly elevated levels of metal  
66 cations, which facilitates the formation of carbonate mineral precipitates even at low concentrations of  
67 carbonate ions (CO<sub>3</sub><sup>2-</sup>) under benign pH conditions.

68 Drawing inspiration from these natural carbon biomineralization mechanisms, this study aims to  
69 develop a biomimetic approach for sustainable carbon mineralization, by engineering microenvironments  
70 that integrate CA catalysis with metal cation concentration. Lumazine synthase from *Aquifex aeolicus*  
71 (AaLS) is an enzyme involved in the biosynthesis of riboflavin.<sup>[26]</sup> Beyond its enzymatic role, AaLS is  
72 known to self-assemble into highly structured, hollow, porous protein nanocages, consisting of 60 identical  
73 AaLS protein subunits, with a diameter of 16 nm.<sup>[27]</sup> An engineered variant of AaLS, termed AaLS-13, has  
74 been developed by introducing 11 specific amino acid mutations – four of which involve amino acids with  
75 acidic side chains located on the inner surface of the nanocage.<sup>[28]</sup> This engineered variant self-assembles  
76 into a 39 nm-wide spherical nanocage with an internal cavity of approximately 15,600 nm<sup>3</sup>.<sup>[29]</sup> More  
77 importantly, these mutations impart a high density of clustered negative charges on the inner surface of the  
78 AaLS-13 nanocage, enabling it to effectively uptake and encapsulate positively charged molecules through  
79 electrostatic interactions.<sup>[30,31]</sup> Leveraging this property, a tagging strategy has been developed to  
80 encapsulate target enzyme cargos within the AaLS-13 nanocages. By fusing the enzyme with a cationic  
81 protein tag, the tag acts as a "zip code", directing the enzyme into the nanocage and anchoring it to the inner  
82 surface with the molecule oriented toward the center of the cavity.<sup>[32]</sup> Various enzymes such as proteases,  
83 retro-alcoholase, β-lactamase, and aldehyde dehydrogenase have been successfully encapsulated into AaLS-

84 13 nanocages by cationic tag fusion.<sup>[33,34]</sup> These unique properties make the AaLS-13 nanocage a promising  
85 platform for mimicking the natural carbon biomineralization process. The nanocage's potential to  
86 encapsulate CA, combined with the possible capability to uptake and concentrate cationic molecules within  
87 its cavity, could offer a synergistic and integrated system for CA catalysis and metal cation concentration.  
88 However, despite this promise, previous AaLS-13 studies have primarily focused on encapsulating highly  
89 positively charged biomolecules, with little known about the encapsulation of small, low positively charged  
90 cations.<sup>[27,32,35,36]</sup> Furthermore, while earlier research has explored AaLS-13's interactions with charged  
91 molecules to manipulate their concentrations within the nanocage and tune the catalysis of encapsulated  
92 enzymes, it has centered on direct substrates for the encapsulated enzymes.<sup>[33,37,38]</sup> This differs  
93 fundamentally from the proposed carbon mineralization application, where the product from the  
94 encapsulated enzyme ( $\text{CO}_3^{2-}$ ) reacts with an indirect substrate (metal cation) within the nanocage,  
95 presenting a novel avenue that requires further exploration.

96 Here, we report on the development of an AaLS-13-based bionanoreactor designed to mimic  
97 natural carbon biomineralization processes for sustainable and efficient mineralization of  $\text{CO}_2$ . We  
98 systematically evaluate the encapsulation of metal cations in AaLS-13 protein nanocages and highlight the  
99 critical role of nanocage's assembled structure in facilitating metal cation interactions, thereby enhancing  
100 their availability for subsequent reactions. Using a new polypeptide tagging approach, we encapsulate CA  
101 into AaLS-13 nanocages and construct AaLS-13-encapsulated CA bionanoreactors that integrate CA  
102 catalysis with metal cation concentration to replicate natural carbon biomineralization mechanisms. We  
103 demonstrate that the bionanoreactors efficiently convert dissolved  $\text{CO}_2$  into carbonate minerals under near-  
104 neutral pH conditions and capture and mineralize atmospheric  $\text{CO}_2$  in the presence of environmentally  
105 relevant levels of metal cations, achieving significantly improved catalytic performance compared to  
106 unencapsulated CA enzyme. This work lays the foundation for developing and applying AaLS-13-based  
107 bionanoreactors for sustainable carbon mineralization, offering an environmentally friendly alternative to  
108 conventional CCS methods. It also provides new insights into harnessing protein nanocage-substrate  
109 interactions to modulate local microenvironments and optimize biochemical reactions, paving the way for

110 future advancements in utilizing AaLS-13 nanocages to fine-tune enzyme catalysis across diverse  
111 biotechnological, biomedical, and environmental applications.

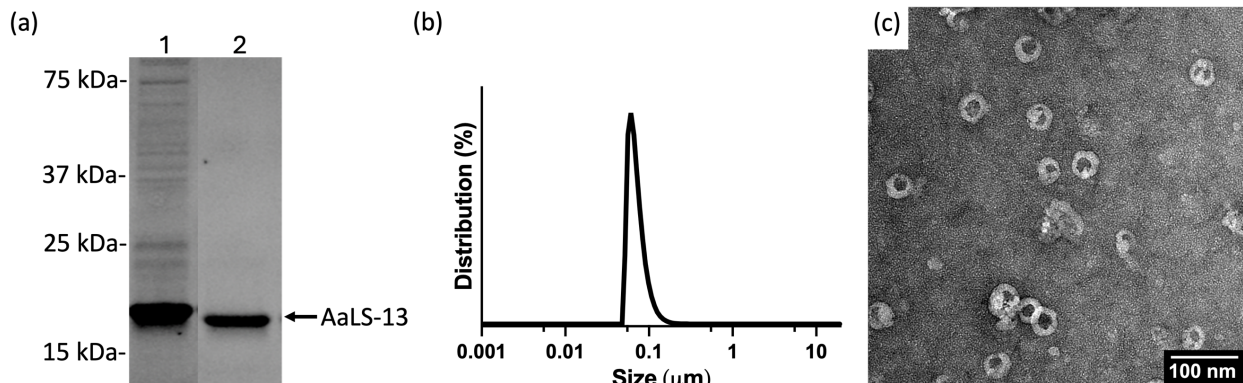
112

113 **2. Results and Discussion**

114 **2.1 AaLS-13 Protein Nanocage Production and Characterization**

115 The AaLS-13 protein was expressed cytoplasmically in *Escherichia coli* and purified from lysed  
116 cells using nickel-nitrilotriacetic acid (Ni-NTA) affinity resins. The successful production and assembly of  
117 purified AaLS-13 protein nanocages were confirmed using sodium dodecyl sulfate-polyacrylamide gel  
118 electrophoresis (SDS-PAGE) and dynamic light scattering (DLS) analyses (Figure 1a & 1b). SDS-PAGE  
119 results showed a prominent band corresponding to the ~17 kDa AaLS-13 protein in both the soluble fraction  
120 post-cell lysis and the Ni-NTA purified eluate, consistent with the expected molecular weight of the AaLS-  
121 13 monomer (16.86 kDa) as calculated from its amino acid sequence.<sup>[28]</sup> DLS measurements revealed a  
122 dominant peak at hydrodynamic diameters of approximately 50 nm (Figure 1b),<sup>[39]</sup> supporting successful  
123 nanocage assembly. To further validate the morphology of the obtained AaLS-13 nanocages, negative-stain  
124 transmission electron microscopy (TEM) was performed, which revealed relatively uniform spherical  
125 particles with average outer diameters of  $42.3 \pm 4.5$  nm (Figure 1c & S1a,b). Taken together, the protein  
126 size, particle size distribution, and morphology of the produced AaLS-13 nanocages aligned well with the  
127 structures reported in previous studies,<sup>[29,31]</sup> indicating successful expression and assembly of the  
128 nanocages.

129



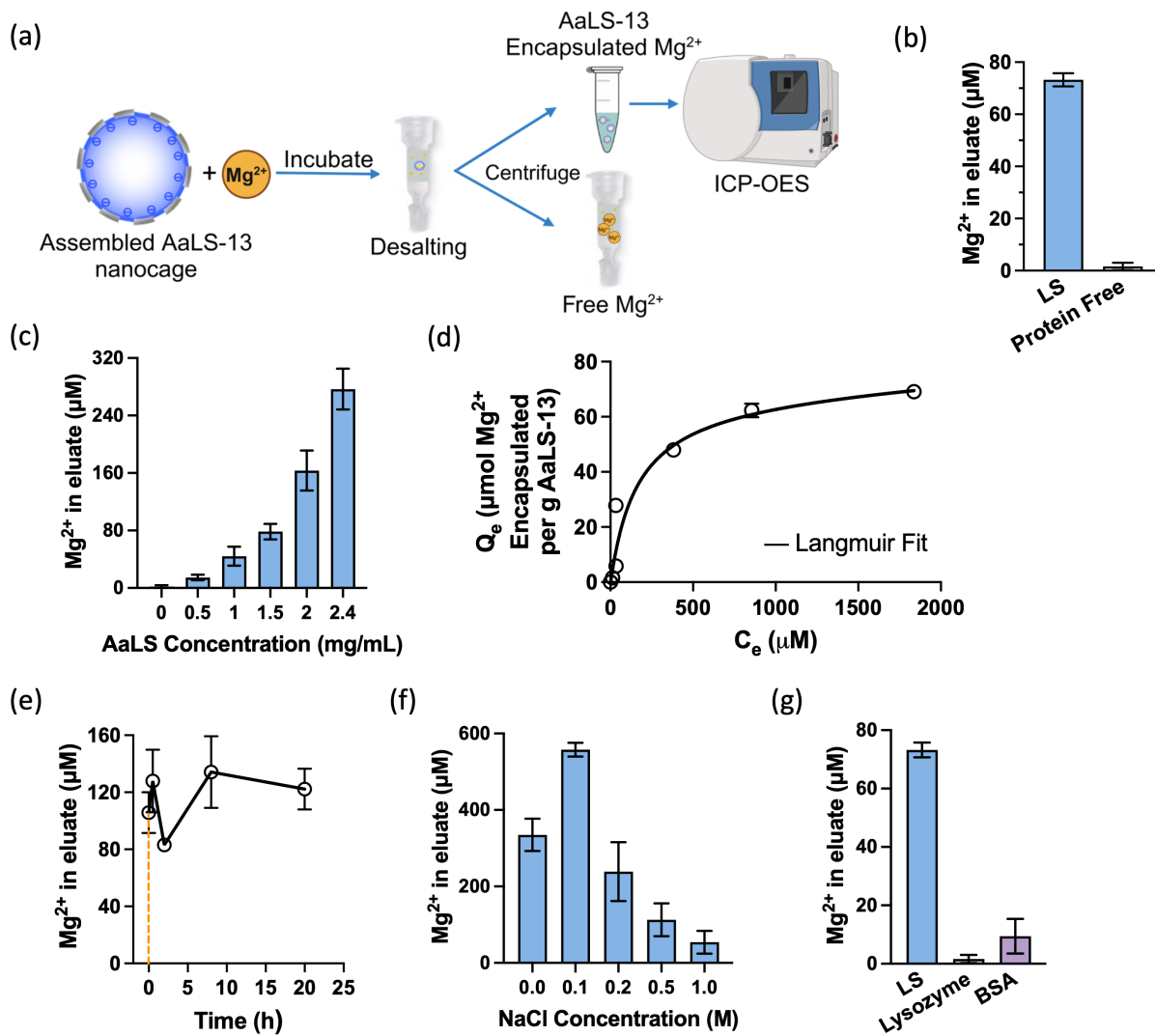
130  
131 **Figure 1.** (a) SDS-PAGE analysis of AaLS-13 expressed in *E. coli* BL21(DE3) cells. Lane 1: supernatant  
132 obtained from the cell lysate after centrifugation; Lane 2: Ni-NTA purified sample from the lysate  
133 supernatant. The AaLS-13 protein band is observed at approximately 17 kDa. (b) DLS size distribution  
134 curve of assembled AaLS-13 nanocages. (c) Negative-stain TEM image of assembled AaLS-13 (5  $\mu$ M  
135 monomer concentration). The stained proteins appear as bright circles against a dark background, with  
136 most of the assembled AaLS-13 nanocages measuring approximately 40 nm in diameter.  
137

## 138 2.2 Metal Cation Encapsulation and Concentration

139 To investigate the cation encapsulation capabilities of the assembled AaLS-13 protein nanocages,  
140 we conducted an incubation study using  $Mg^{2+}$  ions. Magnesium was selected due to its abundant availability  
141 in natural water bodies, especially seawater, making it not only easily accessible but also a low-cost option  
142 for large-scale applications.<sup>[10]</sup> Additionally,  $Mg^{2+}$  readily interacts with dissolved inorganic carbon species  
143 to form stable magnesium carbonate, which is a crucial step in carbon sequestration processes.<sup>[40]</sup> These  
144 properties make  $Mg^{2+}$  an ideal candidate for exploring the potential of AaLS-13 protein nanocages in  
145 biomimetic carbon mineralization. Following incubation, free  $Mg^{2+}$  ions were separated from those  
146 associated with the protein nanocages using spin desalting columns filled with size-exclusion gels. The gels  
147 contain pores that are small enough to trap molecules smaller than 6 kDa, allowing free  $Mg^{2+}$  ions to enter  
148 the gel pores while the AaLS-13-associated  $Mg^{2+}$  ions are eluted with the nanocages during centrifugation  
149 (Figure 2a). The  $Mg^{2+}$  concentration in the eluate was then quantified using Inductively Coupled Plasma  
150 Optical Emission Spectroscopy (ICP-OES). Figure 2b shows that in the presence of AaLS-13 nanocages,  
151 the  $Mg^{2+}$  concentration in the column eluate reached around 75  $\mu$ M, while the protein free control exhibited  
152 only a negligible amount of  $Mg^{2+}$ . This contrast clearly indicates that the AaLS-13 nanocages are capable

153 of effectively taking up  $Mg^{2+}$  ions. When normalized to the AaLS-13 protein concentration, the amount of  
 154 associated  $Mg^{2+}$  equates to about 70  $\mu\text{mol}$  per gram of AaLS-13 protein, corresponding to approximately  
 155 424  $Mg^{2+}$  ions per AaLS-13 nanocage.

156



157  
 158 **Figure 2.** (a) Schematic illustration of evaluating  $Mg^{2+}$  cation encapsulation by AaLS-13 protein  
 159 nanocages.  $Mg^{2+}$  was mixed with assembled AaLS-13 and incubated at room temperature. During  
 160 subsequent centrifugation, the desalting column resin trapped free  $Mg^{2+}$  ions, while  $Mg^{2+}$  encapsulated  
 161 within AaLS-13 nanocages was collected in the flow-through after centrifugation and then quantified by  
 162 ICP-OES. (b) Significant amounts of  $Mg^{2+}$  were detected in the eluate in the presence of AaLS-13  
 163 nanocages, while the protein free control exhibited negligible  $Mg^{2+}$ . Error bars represent the standard  
 164 deviations of three independent experiments. (c)  $Mg^{2+}$  concentration in the desalting column eluate under  
 165 different AaLS-13 concentrations (0, 0.5, 1, 1.5, 2, 2.4 mg/mL). The  $Mg^{2+}$  concentration in the initial  
 166 mixture was 1 mM. Error bars represent the standard deviations of three independent experiments. (d)

167 Encapsulation isotherm of Mg<sup>2+</sup> within AaLS-13 nanocages at a fixed concentration of AaLS-13 (2 mg/mL  
168 in monomer) and different initial concentrations of Mg<sup>2+</sup> ( $C_0 = 0, 5, 20, 100, 500, 1000, 2000 \mu\text{M}$ ). The  
169 curve fits well with the Langmuir isotherm. Error bars represent the standard deviations of three  
170 independent experiments. (e) Mg<sup>2+</sup> concentration in the eluate after incubating with AaLS-13 nanocages  
171 for 0, 0.5, 2, 8, and 20 hours, highlighting that the encapsulation rapidly reached equilibrium. Error bars  
172 represent the standard deviations of three independent experiments. (f) Effect of NaCl on Mg<sup>2+</sup>  
173 encapsulation within AaLS-13. The Mg<sup>2+</sup> concentration in the eluate peaked at a NaCl concentration of 0.1  
174 mM; however, as the NaCl concentration increased or decreased beyond this point, a reduction in Mg<sup>2+</sup>  
175 concentration in the eluate was observed. Error bars represent the standard deviations of three independent  
176 experiments. (g) Comparison of Mg<sup>2+</sup> interactions with AaLS-13, lysozyme (positively charged at neutral  
177 pH), and BSA (negatively charged at neutral pH). Both lysozyme and BSA exhibited significantly lower  
178 interactions with Mg<sup>2+</sup> compared to AaLS-13 nanocages. Error bars represent the standard deviations of  
179 three independent experiments.

180

181 A previous study investigating the interaction between metal cations and ferritin, a protein  
182 nanocage with a negatively charged inner surface similar to AaLS-13 but smaller size, revealed that ferritin-  
183 associated metal could localize either on the outer surface or within the interior cavity, depending on the  
184 metal species.<sup>[41]</sup> The key distinction between these interactions lies in stoichiometric binding. Outer surface  
185 binding relies on a limited number of specific sites forming coordination bonds with metal cations, resulting  
186 in a low stoichiometric of fewer than ten metal cations per ferritin nanocage. In contrast, the interior cavity's  
187 interaction with metal ions primarily occurs through electrostatic interactions, allowing for a significantly  
188 higher stoichiometric binding, with tens of metal ions per ferritin nanocage. Therefore, given that each  
189 AaLS-13 nanocage can take up hundreds of Mg<sup>2+</sup> ions, we reason that these ions are encapsulated within  
190 the nanocage's cavity, like many other cationic molecules.<sup>[32,33,34,42]</sup> Assuming the encapsulated Mg<sup>2+</sup> ions  
191 are uniformly distributed within the cavity, the estimated average concentration of Mg<sup>2+</sup> inside the  
192 nanocages is 45 mM – an enrichment factor of 22.5 times relative to the initial concentration in solution.  
193 This finding suggests that AaLS-13 nanocage encapsulation significantly concentrates Mg<sup>2+</sup> ions within its  
194 cavity.

195 As the concentration of AaLS in the incubation mixture increased, the level of Mg<sup>2+</sup> in the eluate  
196 correspondingly rose (Figure 2c). We then varied the initial concentration of Mg<sup>2+</sup> from 0 to 2000 μM while  
197 maintaining a constant AaLS-13 concentration of 2.4 mg/mL to investigate the isotherm of Mg<sup>2+</sup>

198 encapsulation in AaLS-13 nanocages. As shown in Figure 2d, the encapsulation data fit well with the  
199 Langmuir isotherm, yielding a Langmuir affinity constant of  $6.23 \times 10^3$  M<sup>-1</sup> and a maximum encapsulation  
200 capacity of 70 μmol Mg<sup>2+</sup> per gram of AaLS-13 protein. This affinity constant and maximum capacity are  
201 comparable to, if not better than, those of many other metal ion sorbents such as activated carbon, zeolites,  
202 and silica-based sorbents.<sup>[43,44,45]</sup> Moreover, the encapsulation process reached equilibrium within seconds  
203 (Figure 2e), with Mg<sup>2+</sup> ions remaining bound within AaLS-13 nanocages for hours to days. This rapid  
204 equilibrium contrasts with other proteins used in metal adsorption, such as bovine serum albumin (BSA),  
205 where equilibrium typically requires several hours of incubation.<sup>[46]</sup>

206 Ionic strength was also found to significantly influence Mg<sup>2+</sup> encapsulation. At a NaCl  
207 concentration of 0.1 M, the Mg<sup>2+</sup> concentration in the eluate peaked, indicating the most efficient  
208 encapsulation at this ionic strength (Figure 2f). As the NaCl concentration increased, a decline in Mg<sup>2+</sup>  
209 concentration in the eluate was observed, suggesting that higher ionic strength reduced encapsulation  
210 efficiency. This effect could be due to the electrostatic shielding caused by increased ionic strength,<sup>[47,48]</sup>  
211 which inhibits interactions between the cations and the negatively charged inner surface of the nanocages.  
212 Interestingly, when the NaCl concentration decreased from 0.1 M to 0 M, the Mg<sup>2+</sup> concentration in the  
213 eluate also dropped, despite the lower ionic strength. This unusual phenomenon is possibly related to the  
214 structural properties of AaLS-13 nanocages. Previous studies have shown that the assembly of AaLS-13  
215 nanocages is sensitive to salt concentration, with fully intact assemblies maintained at NaCl concentrations  
216 of  $\geq 150$  mM, and partial disassembly occurring at lower salt concentrations.<sup>[27]</sup> Thus, at 0 M NaCl, the  
217 AaLS-13 nanocages likely partially disassembled, weakening their interactions with Mg<sup>2+</sup> ions and  
218 reducing the efficiency of Mg<sup>2+</sup> encapsulation. This observation underscores the critical importance of  
219 nanocage structural integrity in effective metal cation encapsulation.

220 To further confirm the role of the AaLS-13 nanocage structure in its Mg<sup>2+</sup> encapsulation capability,  
221 we conducted additional adsorption experiments using two other proteins: lysozyme and BSA. Lysozyme,  
222 a positively charged protein at neutral pH (~7.4) with an approximate charge of +7.2 per protein (Figure  
223 S2b), showed minimal interaction with Mg<sup>2+</sup> ions, as evidenced by the lack of increase in Mg<sup>2+</sup>

concentration in the eluate (Figure 2g). This result is not surprising due to the electrostatic repulsion between the similarly charged lysozyme and Mg<sup>2+</sup> ions. In contrast, BSA, which carries a similar net negative charge as the AaLS-13 protein monomer at neutral pH (Figure S2a & c) and would theoretically attract Mg<sup>2+</sup> cations, only slightly increased the Mg<sup>2+</sup> concentration in the eluate to 6 μM, 13 folds lower than those achieved with AaLS-13 nanocages. This significant difference underscores the crucial role of the assembled nanocage structure of AaLS-13 in enhancing its interaction with Mg<sup>2+</sup> ions. Sasaki et al. calculated the electrostatic surface potential of an AaLS-13 pentamer, revealing that the majority of its negative charge is concentrated on the inner surface.<sup>[31]</sup> The assembly of the AaLS-13 nanocage thus creates a highly clustered array of negative charges, which leads to stronger electrostatic attraction and facilitates the effective encapsulation of positively charged Mg<sup>2+</sup> ions within the nanocages. This enhancement of electrostatic interactions is consistent with the findings of Zhou and Pang, who demonstrated that clustering-like charges on a protein surface generate strong local electric fields, thereby improving the binding affinity for oppositely charged ions and molecules.<sup>[49]</sup> Similarly, the study by Sheinerman and Honig showed that clustered charges at protein-protein interfaces create strong electrostatic fields, which promote interaction by attracting oppositely charged residues on interacting molecules.<sup>[50]</sup>

239

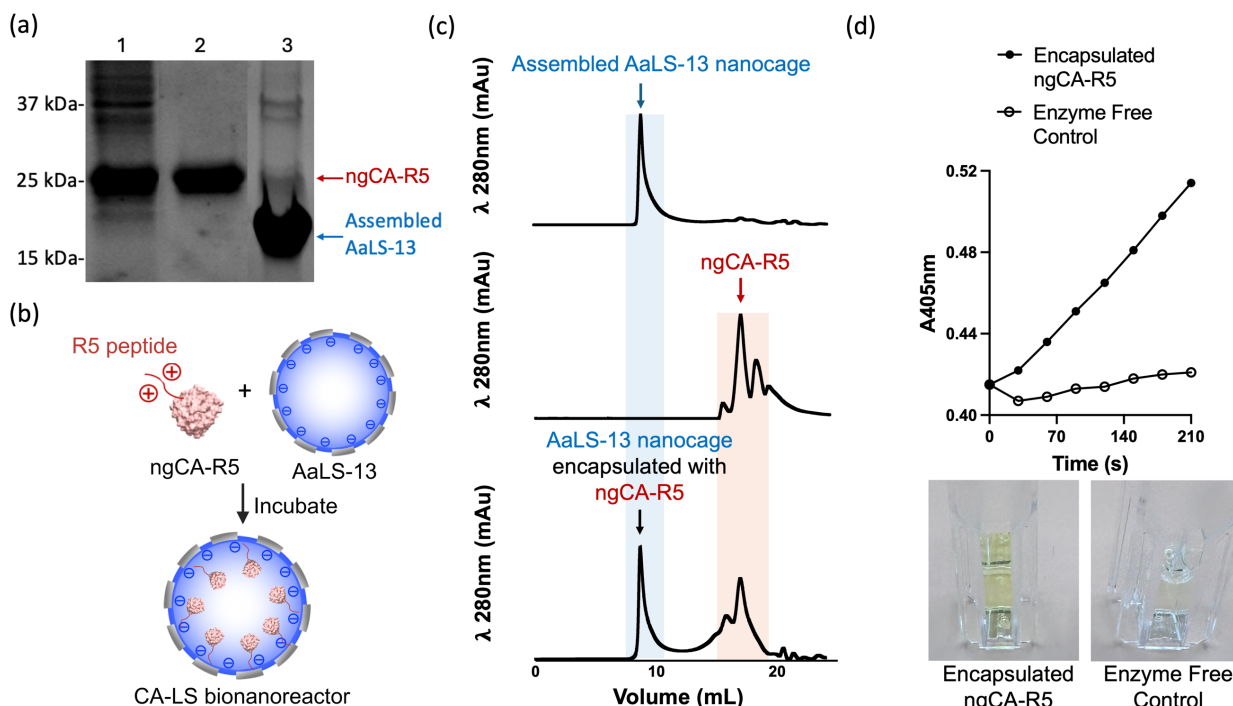
### 240 **2.3 Encapsulation of CA**

Building on the effective charge-based interactions between AaLS-13 and Mg<sup>2+</sup>, we proceeded to construct the enzyme-protein nanocage bionanoreactors by encapsulating CA from *Neisseria gonorrhoeae* (ngCA) – one of the fastest CAs known – within AaLS-13 nanocages.<sup>[51]</sup> To facilitate interaction with the negatively charged inner surface of AaLS-13, the ngCA enzyme was fused with a polycationic R5 peptide. While previous studies have successfully encapsulated a variety of enzymes within AaLS-13 by attaching them with a supercharged GFP(+36) tag,<sup>[27,29,52]</sup> we found that this tag caused low elution yields of ngCA from the Ni-NTA column. This is likely due to the large size of GFP(+36) (~27.5 kDa), which may interfere with the folding of the tagged ngCA or its interaction with the Ni-NTA resin. Thereby, we considered the polycationic R5 peptide as a more suitable alternative, due to its significantly smaller size (~2.5 kDa). The

250 R5 tag is derived from silaffins, a class of proteins that play crucial roles in forming silica cell walls in  
251 diatoms. Specifically, R5 corresponds to a repeat unit within silaffins that effectively catalyzes the  
252 polymerization of negatively charged silica precursors through electrostatic interactions.<sup>[53]</sup>

253 The successful production and purification of R5-tagged ngCA (ngCA-R5) were confirmed by  
254 SDS-PAGE analysis (Figure 3a), where the fused protein appeared as a distinct band at approximately 25  
255 kDa, consistent with its predicted molecular weight based on the amino acid sequence.<sup>[54]</sup> Subsequently,  
256 the purified ngCA-R5 was incubated overnight with pre-purified AaLS-13 nanocages at room temperature  
257 to facilitate encapsulation (Figure 3b), and the mixture was then subjected to size exclusion chromatography  
258 (SEC) fractionation to separate free and AaLS-13-encapsulated ngCA-R5. As shown in Figure 3c, the  
259 AaLS-13 nanocage, due to its large size, eluted early with a sharp peak around 9 mL, while unencapsulated  
260 ngCA-R5 eluted in a broader peak between 17 and 22 mL. When the encapsulation mixture was loaded  
261 onto the SEC column, the elution profile revealed two distinct peaks: a sharp peak for AaLS-13 nanocages  
262 and a broad peak for unencapsulated ngCA-R5. Subsequent SDS-PAGE analysis of the AaLS-13 elution  
263 fraction revealed two bands corresponding to the protein size of AaLS-13 and ngCA-R5 (Figure 3a, lane  
264 3), indicating successful encapsulation of ngCA-R5 within AaLS-13 nanocages. To further validate this,  
265 we assessed the CA activity of the AaLS-13 fraction using p-nitrophenyl acetate (pNPA) and phenol red  
266 assays. The pNPA assay measures the enzyme's ability to catalyze the hydrolysis of pNPA to p-nitrophenol,  
267 a yellow product that absorbs strongly at 405 nm.<sup>[55]</sup> As shown in Figure 3d, the AaLS-13 fraction  
268 significantly promoted the absorbance increase at 405 nm, suggesting the presence of active ngCA-R5.  
269 Likewise, the phenol red assay, which tracks the pH shift resulting from the conversion of dissolved CO<sub>2</sub>  
270 to bicarbonate, also confirmed the presence of active CA by the observed accelerated decrease in  
271 absorbance at 560 nm (Figure S3a & b). Collectively, these results demonstrated that the R5 tag effectively  
272 directs the encapsulation of ngCA into AaLS-13, and more importantly, that the AaLS-13-encapsulated  
273 enzyme remained catalytically active, which is crucial for the subsequent studies on using the enzyme-  
274 protein nanocage bionanoreactors for carbon sequestration.

275



276

277 **Figure 3.** (a) SDS-PAGE analysis of *E. coli* cell lysate supernatant containing ngCA-R5 (lane 1), Ni-NTA  
 278 purified ngCA-R5 (lane 2), and SEC-purified CA-LS bionanoreactors (lane 3). The red arrow indicates the  
 279 ngCA-R5 band (~25 kDa), and the blue arrow indicates AaLS-13 protein (~17 kDa). (b) Schematic  
 280 illustration of the construction of CA-LS bionanoreactors through incubating assembled AaLS-13 nanocage  
 281 with ngCA fused to a polycationic R5 peptide. The clustered negative charge on the inner surface of AaLS-  
 282 13 nanocage attracts ngCA-R5 and encapsulates the enzyme within its cavity. (c) SEC elution profiles of  
 283 assembled AaLS-13 nanocage, free ngCA-R5, and the encapsulation mixture of AaLS-13 nanocage and  
 284 ngCA-R5 (top to bottom) using a Superose 6 Increase 10/300 GL column. Arrows indicate the eluate  
 285 fractions corresponding to the proteins of interest. The blue bar marks the elution fraction of assembled  
 286 AaLS-13 (~9 mL), with or without ngCA-R5 encapsulated, while the orange bar marks the elution fraction  
 287 of ngCA-R5 (~17 mL). (d) Evaluation of the catalytic activity of SEC-purified CA-LS bionanoreactors  
 288 containing encapsulated ngCA-R5 using a pNPA hydrolysis assay. CA catalyzes pNPA hydrolysis, forming  
 289 p-nitrophenol, a yellow compound with strong absorbance at 405 nm. An enzyme free control was  
 290 performed under the same experimental conditions but without CA-LS.  
 291

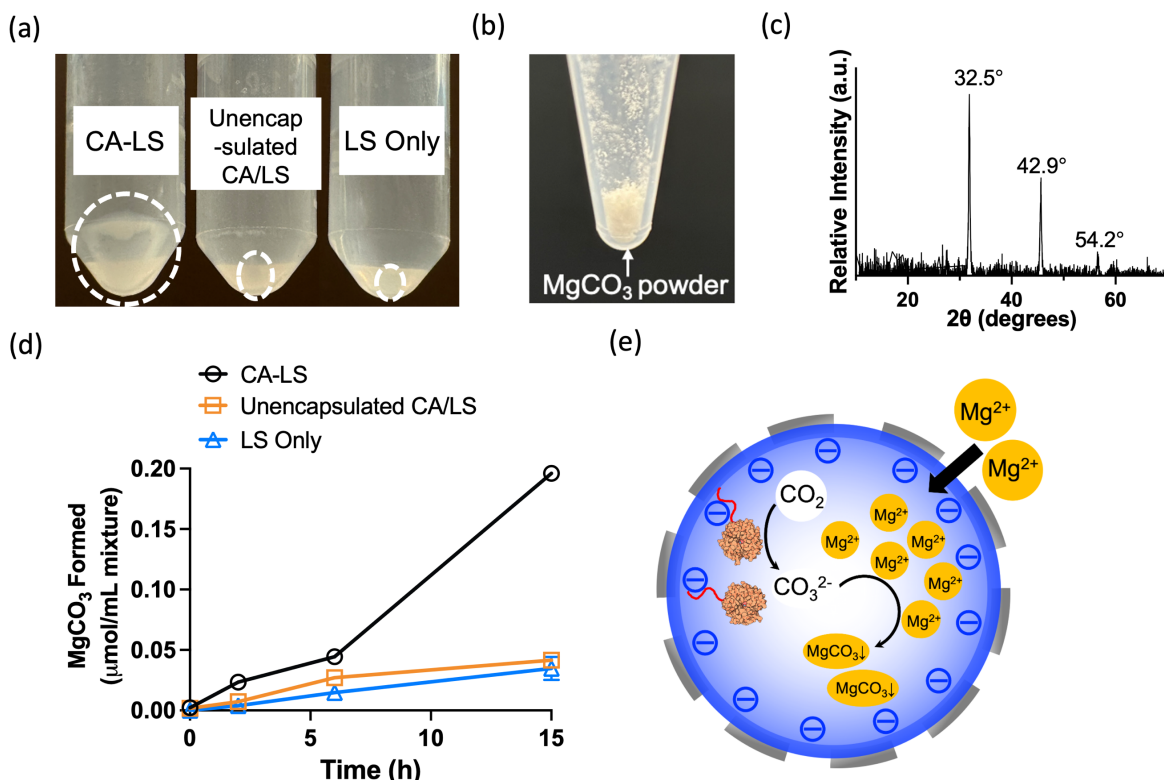
## 292 2.4 Bionanoreactor for CO<sub>2</sub> Mineralization

293 We next evaluated the efficacy of the AaLS-13 nanocages encapsulating ngCA-R5 (CA-LS) as  
 294 bionanoreactors for catalyzing the direct mineralization of dissolved CO<sub>2</sub> with Mg<sup>2+</sup> ions. The purified CA-  
 295 LS bionanoreactors were incubated with 1 mM MgCl<sub>2</sub> and 5.6 mM CO<sub>2</sub> in a pH 8.0 buffer at room  
 296 temperature with continuous shaking. After overnight incubation, the mixture turned cloudy with the  
 297 formation of white precipitate particles. Centrifugation resulted in a substantial white pellet at the bottom

298 of the tube (Figure 4a), which was dried and subjected to X-ray diffraction (XRD) analysis to confirm the  
299 identity of the precipitate and determine its crystalline phases (Figure 4b). As shown in Figure 4c, the XRD  
300 pattern displayed three sharp peaks at  $2\theta$  values of  $32.5^\circ$ ,  $42.9^\circ$ , and  $54.2^\circ$ , which correspond to the  
301 characteristic peaks of anhydrous  $\text{MgCO}_3$ <sup>[56]</sup> confirming the mineralization of dissolved  $\text{CO}_2$  into  
302 crystalline  $\text{MgCO}_3$  under the catalysis of CA-LS bionanoreactors. The absence of peaks corresponding to  
303 other Mg-containing phases such as  $\text{Mg(OH)}_2$  suggests a high selectivity of the bionanoreactors for  $\text{MgCO}_3$   
304 formation. In contrast, a control experiment using only AaLS-13 without CA (LS only) remained clear at  
305 the end of incubation and produced negligible pellets after centrifugation (Figure 4a). This result was  
306 expected as the hydration of dissolved  $\text{CO}_2$  at pH 8.0 is slow, limiting the availability of carbonate ions and  
307 preventing the formation of  $\text{MgCO}_3$  precipitates. However, interestingly, when a mixture of CA (not fused  
308 to R5) and AaLS-13 was tested (unencapsulated CA/LS), the solution stayed clear after overnight  
309 incubation, and only a minimal pellet was obtained (Figure 4a).

310 To quantitatively determine and compare the amount of  $\text{MgCO}_3$  formed, we dissolved the collected  
311 pellets in nitric acid and measured the  $\text{Mg}^{2+}$  concentrations using ICP-OES. Figure 4d shows the time-  
312 dependent formation of  $\text{MgCO}_3$  precipitates for the bionanoreactor experimental group and two control  
313 groups. After two hours of reaction, CA-LS nanoreactors produced 0.02  $\mu\text{mol}$  of  $\text{MgCO}_3$  per mL reaction  
314 mixture, corresponding to the mineralization of 0.02  $\mu\text{mol}$   $\text{CO}_2$ , which is 6 times higher than the amount  
315 achieved by the LS only and unencapsulated CA/LS controls. As the reaction progressed, the production of  
316  $\text{MgCO}_3$  increased across all three groups, albeit at different rates. From 6 to 15h, the CA-LS  
317 bionanoreactors exhibited a significant growth of  $\text{MgCO}_3$  precipitation, ultimately reaching 0.2  $\mu\text{mol}$ ,  
318 equivalent to 0.2  $\mu\text{mol}$   $\text{CO}_2$  captured per mL mixture. This rate is approximately 5 times higher than that  
319 observed in two control groups.

320



321  
322 **Figure 4.** (a) Precipitates formed by CA-LS, unencapsulated CA/LS, and LS only control in the presence  
323 of Mg<sup>2+</sup> and dissolved CO<sub>2</sub>. White dashed circles indicate the pellets collected at the bottom of the tubes  
324 after centrifugation. (b) Desiccator-dried powder of the CA-LS formed precipitates, which appear as fine,  
325 white crystalline particles. (c) XRD analysis of the dried precipitate formed by CA-LS. Peaks at 2θ values  
326 of 32.5°, 42.9°, and 54.2° corresponded to the characteristic peaks of anhydrous MgCO<sub>3</sub><sup>[56]</sup> (d) CA-LS  
327 bionanoreactors demonstrated significantly faster and more efficient CO<sub>2</sub> mineralization, as indicated by  
328 the formation of MgCO<sub>3</sub>, compared to both the unencapsulated CA/LS and LS only controls. The MgCO<sub>3</sub>  
329 formation was quantified based on Mg<sup>2+</sup> amounts in the precipitate, calculated at a 1:1 molar ratio. Error  
330 bars represent the standard deviations of three independent experiments. (e) Schematic illustration of  
331 synergistic CO<sub>2</sub> hydration and mineralization reactions within the CA-LS bionanoreactors. Dissolved CO<sub>2</sub>  
332 enters the CA-LS nanocage, where encapsulated ngCA-R5 catalyzes its conversion to carbonate species.  
333 These carbonate species then react with Mg<sup>2+</sup> ions, which are locally concentrated through electrostatic  
334 interactions with the negatively charged inner surface of AaLS-13 nanocages, leading to the accelerated  
335 formation of MgCO<sub>3</sub> precipitates.

336

337 These findings indicate that simply mixing unencapsulated CA with AaLS-13 nanocages has only  
338 a limited effect on carbon mineralization with Mg<sup>2+</sup>, underscoring the importance of CA encapsulation  
339 within AaLS-13 for efficient MgCO<sub>3</sub> precipitation. In a pH 8 buffer, although unencapsulated CA can  
340 catalyze the hydration of CO<sub>2</sub>, only 0.46% of the hydrated CO<sub>2</sub> stays in the CO<sub>3</sub><sup>2-</sup> form, with the majority  
341 being bicarbonate, according to the carbonate equilibria. This low level of carbonate ions resulted in a small

342 reaction quotient of the carbon mineralization reaction ( $\text{CO}_3^{2-} + \text{Mg}^{2+} \rightarrow \text{MgCO}_3$ ), making  $\text{MgCO}_3$   
343 precipitation less favorable. The superior performance of the CA-LS bionanoreactor can be attributed to  
344 the synergy between AaLS-13 and encapsulated ngCA-R5, likely creating a specific microenvironment that  
345 facilitated the formation of  $\text{MgCO}_3$ . As illustrated in Figure 4e, the uptake of  $\text{Mg}^{2+}$  by the AaLS-13  
346 nanocage increases the local  $\text{Mg}^{2+}$  concentration within the cavity, while simultaneously, the encapsulated  
347 ngCA-R5 catalyzes the hydration of dissolved  $\text{CO}_2$  to produce carbonate species. This could lead to an  
348 overlap of “hotspots” for  $\text{Mg}^{2+}$  and carbonate ions within the nanocage, thereby enhancing the formation  
349 of  $\text{MgCO}_3$  precipitates and the mineralization of  $\text{CO}_2$ . In addition, this synergy provides an additional piece  
350 of evidence supporting the successful encapsulation of ngCA-R5 into AaLS-13 nanocages.

351 The ability of the CA-LS bionanoreactor to effectively facilitate carbon mineralization with  $\text{Mg}^{2+}$   
352 at near-neutral pH is particularly noteworthy. Most existing methods often require a high pH (>10) to  
353 overcome the kinetic and thermodynamic constraints of  $\text{CO}_2$  hydration and mineralization reactions,<sup>[57]</sup>  
354 typically relying on alkaline chemicals or electrochemical catalysis, which not only consume significant  
355 amounts of chemicals or energy but can also have adverse effects on aquatic ecosystems.<sup>[58]</sup> In contrast, the  
356 CA-LS bionanoreactor emulates natural carbon biomimetic processes by combining metal ion  
357 concentration with biocatalytic  $\text{CO}_2$  hydration. This integration allows effective carbon mineralization at a  
358 near-neutral pH of 8.0, providing a more eco-friendly and efficient solution for sustainable carbon  
359 sequestration.

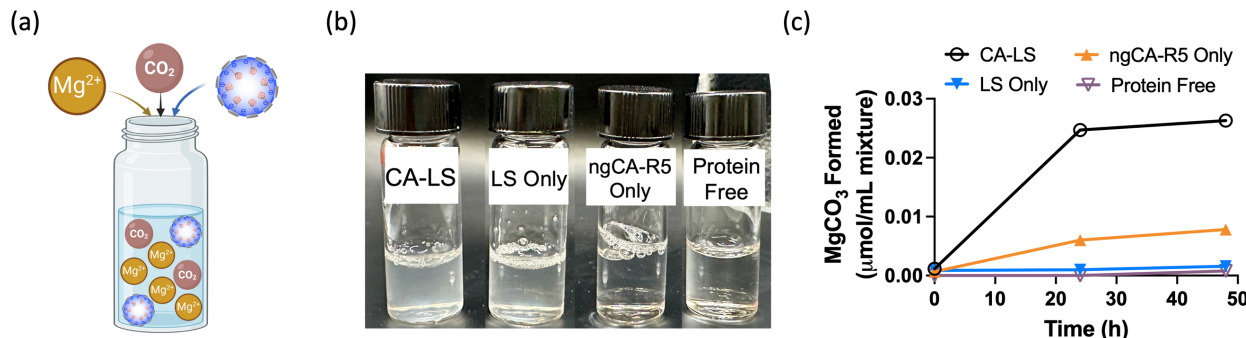
360

## 361 **2.5 Direct $\text{CO}_2$ Capture from Ambient Air**

362 DAC is an increasingly vital technology in the combat against climate change, drawing significant  
363 attention as a key method for reducing atmospheric  $\text{CO}_2$  levels.<sup>[59]</sup> Unlike traditional carbon capture  
364 approaches that focus on concentrated sources, DAC targets  $\text{CO}_2$  directly from the ambient air, thus  
365 complementing existing mitigation strategies and contributing to long-term net-zero goals.<sup>[60]</sup> In light of  
366 this significance, we then evaluated the performance of our CA-LS bionanoreactor in the context of DAC,  
367 aiming to assess its effectiveness in this emerging and crucial area of carbon management. As depicted in

368 Figure 5a, we mixed CA-LS bionanoreactors with 40 mM MgCl<sub>2</sub> in a pH 8.0 buffer within glass vials with  
 369 a loose cap to facilitate CO<sub>2</sub> transfer from the air. The 40 mM Mg<sup>2+</sup> concentration was selected to reflect  
 370 levels commonly found in natural water bodies, such as seawater and groundwater, which are potential  
 371 cost-effective sources of Mg<sup>2+</sup> for large-scale DAC applications.<sup>[9,61]</sup> Three controls containing only ngCA-  
 372 R5, only AaLS-13 nanocages (LS only), and neither ngCA-R5 nor AaLS-13 (protein free) were also  
 373 prepared similarly. At time zero, the CA-LS and LS only groups exhibited a milky appearance due to the  
 374 presence of the assembled nanocages, while the ngCA-R5 only and protein free control groups remained  
 375 crystal clear. After 24h of incubation, cloudiness first appeared in the CA-LS group due to the formation of  
 376 white precipitate particles, with no significant changes observed in the other groups. By 48h, the cloudiness  
 377 in the CA-LS group had intensified, and the ngCA-R5 only group began to show slight cloudiness. In  
 378 contrast, the LS only and protein free groups showed no visible changes (Figure 5b). ICP-OES analysis of  
 379 the pellets collected after centrifugation confirmed that the CA-LS bionanoreactor significantly  
 380 outperformed the three control groups, producing approximately 0.03 μmol of MgCO<sub>3</sub> (equivalent to 0.03  
 381 μmol CO<sub>2</sub> mineralized) per mL mixture, which was 4 times higher than the ngCA-R5 only group and 24  
 382 times higher than the LS only group at the 24h mark (Figure 5c). The protein free control did not generate  
 383 any detectable MgCO<sub>3</sub> precipitation.

384



385  
 386 **Figure 5.** (a) Schematic illustration of direct air capture setup using the CA-LS bionanoreactor and Mg<sup>2+</sup>  
 387 system. Mg<sup>2+</sup> and CA-LS bionanoreactor were combined in a glass vial with a loose cap, allowing  
 388 atmospheric CO<sub>2</sub> to enter and dissolve in the solution over time while minimizing solution evaporation. (b)  
 389 Pictures comparing CA-LS, LS only, ngCA-R5 only, protein free vials with the presence of Mg<sup>2+</sup> after  
 390 exposing to the air for 48h. The CA-LS vial exhibits a significant increase in solution cloudiness compared  
 391 to other groups. (c) MgCO<sub>3</sub> precipitate formation in CA-LS, ngCA-R5 only, LS only, and protein free

392 groups upon air exposure over time, demonstrating the significantly higher efficiency of CA-LS  
393 bionanoreactors in capturing and mineralizing atmospheric CO<sub>2</sub>. Error bars represent the standard  
394 deviations of three independent experiments.

395

396 The CA-LS bionanoreactor's capacity to capture CO<sub>2</sub> directly from the air presents substantial  
397 opportunities for integrating this technology into DAC systems. While biomimetic carbon mineralization  
398 with CA has been widely studied, most research has focused on concentrated CO<sub>2</sub> sources or post-  
399 combustion gases rather than ambient atmospheric CO<sub>2</sub>.<sup>[62,63]</sup> This focus is largely due to the low  
400 concentration of CO<sub>2</sub> in the atmosphere (~0.04%) compared to more concentrated CO<sub>2</sub> streams, which  
401 results in significantly lower carbonate concentrations.<sup>[64]</sup> This low concentration challenges the efficient  
402 formation of carbonates and makes substantial mineral carbonate precipitation from atmospheric CO<sub>2</sub>  
403 difficult, especially at near-neutral pH. In contrast, as described above, the CA-LS bionanoreactor could  
404 overcome this limitation by combining the effects of AaLS-13 to concentrate Mg<sup>2+</sup> ions with the biocatalytic  
405 activity of encapsulated ngCA-R5 to facilitate CO<sub>2</sub> hydration. This synergy enhances MgCO<sub>3</sub> formation  
406 and the mineralization of atmospheric CO<sub>2</sub>, making the CA-LS bionanoreactor a more sustainable solution  
407 for DAC compared to other methods that require more stringent conditions.<sup>[65]</sup>

408

### 409 3. Conclusions

410 In summary, this study develops and demonstrates a bionanoreactor approach based on AaLS-13  
411 nanocages and CA enzyme to enable effective carbon mineralization under mild, ambient conditions. The  
412 assembled AaLS-13 nanocage, with its highly negatively charged interior surface, exhibits a strong capacity  
413 and affinity for uptaking Mg<sup>2+</sup> ions from surrounding solutions, concentrating them within its cavity.  
414 Notably, the uptake efficiency is dependent on salt concentration, peaking at 0.1 mM NaCl and decreasing  
415 at both lower and higher NaCl levels. This pattern suggests the critical role of AaLS-13 nanocage's  
416 assembled structure in facilitating metal cation interactions, thereby enhancing their availability for  
417 subsequent reactions. By encapsulating the CA enzyme tagged with a cationic polypeptide, the resulting  
418 CA-LS bionanoreactors retain their catalytic activity, demonstrating effectiveness in p-NPA hydrolysis and

419 CO<sub>2</sub> hydration. Leveraging the catalytic capabilities of the CA-LS bionanoreactors alongside their ability  
420 to concentrate Mg<sup>2+</sup>, these bionanoreactors achieve significantly accelerated rates of CO<sub>2</sub> mineralization.  
421 They are capable of mediating the mineralization of CO<sub>2</sub> from solutions while also effectively capturing  
422 and mineralizing atmospheric CO<sub>2</sub> at near-neutral pH in the presence of metal cations. Collectively, these  
423 findings lay a foundation for utilizing protein nanocage-based enzyme bionanoreactors for sustainable  
424 carbon mineralization, presenting an environmentally friendly alternative to traditional CCS and DAC  
425 approaches. In addition, this work provides new insights into leveraging protein nanocage-substrate  
426 interactions to modulate local microenvironments and enhance biochemical reactions, which could inform  
427 future advancements in the use of AaLS-13 protein nanocages to fine-tune enzyme catalysis, with potential  
428 applications across diverse biotechnological, biomedical, and environmental fields.

429 **4. Experimental Section**

430 *Production and Purification of AaLS-13 and ngCA-R5*

431       The DNA sequence for ngCA, including a 6×His tag, was codon-optimized for expression in *E.*  
432 *coli* and purchased in a pET-21b+ expression vector (ngCA-6His-pET21b+) from GenScript. An R5 peptide  
433 (Ser-Ser-Lys-Lys-Ser-Gly-Ser-Tyr-Ser-Gly-Ser-Lys-Gly-Ser-Lys-Arg-Arg-Ile-Leu) coding sequence was  
434 inserted between ngCA and 6×His using the Q5 site-directed mutagenesis kit from New England Biolabs,  
435 with custom primers R5-F and R5-R (Table S1) ordered from Azenta. The constructed plasmid (ngCA-R5-  
436 6His-pET21b+) was amplified in *E. coli* DH5α cells (New England Biolabs) and verified through Sanger  
437 sequencing. Additionally, the gene encoding AaLS-13 with a 6×His tag was synthesized based on its amino  
438 acid sequence,<sup>[28]</sup> codon optimized for *E. coli* expression, and purchased in a pET-28b+ expression vector  
439 (AaLS-13-6His-pET28b+) from GenScript.

440       Subsequently, ngCA-R5-6His-pET21b+ and AaLS-13-6His-pET28b+ vectors were transformed  
441 into *E. coli* BL21(DE3) cells (New England Biolabs), and protein expression was carried out following  
442 standard protocols. Briefly, positive transformants were first grown overnight in lysogeny broth (LB)  
443 medium supplemented with antibiotics (50 µg/mL ampicillin for ngCA-R5-6His-pET21b+ and 30 µg/mL  
444 kanamycin for AaLS-13-6His-pET28b+). Two ml of the overnight culture was then used to inoculate 200  
445 mL of fresh LB medium, which was incubated at 37 °C, 250 rpm until an OD<sub>600</sub> of 0.6-0.8 was reached.  
446 Protein expression was induced by adding 1 mM isopropyl β-D-1-thiogalactopyranoside (IPTG), and for  
447 ngCA expression, 0.1 mM zinc chloride (ZnCl<sub>2</sub>) was also added. Following induction, cultures were grown  
448 at 20 °C, 250 rpm for 20 hours. Cells were harvested by centrifugation at 4 °C, 12,000 × g for 10 minutes,  
449 and the collected cell pellets were stored at -80 °C until use.

450       For protein extraction, frozen cells were resuspended in 5 volumes of HEPES buffer (50 mM, pH  
451 8.0, 5% glycerol) containing SIGMAFAST EDTA-free protease inhibitor cocktail (Millipore Sigma). Cell  
452 lysis was conducted on ice using a Branson Sonifier 550 in pulse mode with 10% intensity, with 50 ms on  
453 and 50 ms off intervals. The procedure involved ten 30-second cycles of sonication, with a 30-second pause

454 between each cycle to prevent overheating. The crude cell lysate was centrifuged at 20,000 × g for 20  
455 minutes at 4 °C, and the resulting supernatant, containing soluble target proteins, was collected and then  
456 purified using Hispur Ni-NTA affinity resins (Thermo Fisher Scientific) according to the manufacturer's  
457 protocol. In brief, the supernatant was loaded onto a pre-equilibrated Ni-NTA column, which selectively  
458 binds to the 6×His-tagged proteins. After binding, the column was washed with a wash buffer (50 mM  
459 HEPES, pH 8.0, 300 mM NaCl, and 20 mM imidazole) to remove non-specifically bound proteins and  
460 other contaminants. The bound 6×His-tagged proteins were eluted using an elution buffer containing 50  
461 mM HEPES, pH 8.0, 300 mM NaCl, and 250 mM imidazole. The eluted fractions were collected, analyzed  
462 for protein purity using SDS-PAGE, and further desalting using PD-10 desalting columns (Cytiva) to remove  
463 imidazole. The purified ngCA-R5 was stored at 4 °C in HEPES buffer (50 mM, pH 8.0), and the purified  
464 AaLS-13 was left at room temperature to assemble in 50 mM, pH 8.0 HEPES buffer with 5 mM EDTA and  
465 10% 5 M NaCl for at least a week. Protein concentrations in the purified samples were determined using a  
466 bicinchoninic acid (BCA) assay kit (Thermo Fisher Scientific) following the manufacturer's protocol.

467

468 *SEC Purification of Assembled AaLS-13 Nanocages and CA-LS Bionanoreactors*

469 Assembled AaLS-13 protein nanocages and CA-LS bionanoreactors were purified using an NGC  
470 Quest 10 fast protein liquid chromatography (FPLC) system (Bio-rad) equipped with a HiPrep 16/60  
471 Sephadryl S-400 HR column (Cytiva) for AaLS-13 and a Superose 6 Increase 10/300 GL column (Cytiva)  
472 for CA-LS. Protein samples ranging from 250 µL to 5 mL were loaded onto the columns, and SEC was  
473 performed using SEC buffer (50 mM HEPES, 200 mM NaCl, pH 8.0) at a flow rate of 1 mL/min at 4 °C.  
474 UV-Vis absorbance at 280 nm was monitored to detect protein elution, and all fractions were collected for  
475 further analysis by SDS-PAGE.

476

477 *SDS-PAGE Analysis*

478 SDS-PAGE was performed using Any kD mini-PROTEAN TGX stain-free protein gels in the  
479 Tris/Tricine/SDS Running Buffer (Bio-rad). For each sample, 45 µL was mixed with 15 µL of 4× sample  
480 buffer and heated at 95 °C for 5 min. After vortexing, 20 µL of the heated sample was loaded onto the gel.  
481 Electrophoresis was carried out at a constant voltage of 150 V for approximately 45 minutes at room  
482 temperature. Unstained Precision Plus Protein Standards (Bio-rad) were used as molecular weight markers.  
483 The gel was visualized using an Azure 300 gel imaging system.

484

485 *DLS Analysis*

486 Sizing and polydispersity measurements of AaLS-13 nanocages were performed using a Beckman  
487 Coulter Particle Size Analyzer at room temperature. Assembled AaLS-13 samples were diluted to a protein  
488 concentration of 1 mg/mL in 50 mM HEPES buffer (pH 8.0), filtered through 0.22µm low protein retention  
489 membrane, and immediately subjected to DLS analysis.

490

491 *Negative Stain TEM*

492 Purified, assembled AaLS-13 nanocages were prepared for negative-stain TEM by diluting the  
493 sample to a concentration of 5 µM in 50 mM HEPES buffer (pH 8.0). Copper grids (200 mesh, pure carbon  
494 film with no Formvar, PELCO) were utilized for sample preparation. The grid was carefully placed onto  
495 20 µL of the protein solution and incubated for 2 minutes to allow sufficient adsorption. Excess liquid was  
496 then removed by wicking with filter paper. The grid then was briefly rinsed in 0.22 µm membrane-filtered  
497 deionized (DI) water for 1 minute and wicked again with filter paper. This rinsing process was repeated  
498 three times. Subsequently, staining was performed by placing the grid onto 20 µL of 2% uranyl acetate  
499 solution and incubating for an additional 2 minutes. The excess stain was removed using filter paper, and  
500 the grid was air-dried before being stored at room temperature for imaging. TEM images were captured  
501 using a Hitachi H9500 transmission electron microscope operating at 200 kV at the Nanoscale Fabrication  
502 and Characterization Facility (NFCF) at the University of Pittsburgh.

503

504      *Evaluation of Mg<sup>2+</sup> Encapsulation within AaLS-13 Protein Nanocage*

505           Purified, assembled AaLS-13 nanocages were mixed with varying concentrations of MgCl<sub>2</sub> in 50  
506 mM, pH 8.0 HEPES buffer. Different concentrations of AaLS-13 and NaCl, as well as varying incubation  
507 times, were tested. After incubation, 60 µL samples were processed using Bio-Rad Micro Bio-Spin 6  
508 desalting columns (the columns were pre-prepared by centrifuging at 1000 × g for 2 min to remove buffer).  
509 The sample mixture was loaded onto the columns, where free Mg<sup>2+</sup> ions were retained by the resin, while  
510 Mg<sup>2+</sup> ions encapsulated within the AaLS-13 nanocages were eluted after centrifugation at 1000 × g for 4  
511 minutes. The flow-through fraction was collected and mixed with an acidic buffer (50 mM HEPES + 1%  
512 nitric acid) for quantitative magnesium analysis using ICP-OES.

513

514      *Preparation of CA-LS Bionanoreactors*

515           Assembled AaLS-13 nanocages were mixed with purified ngCA-R5 in 50 mM HEPES buffer (pH  
516 8.0), maintaining a final AaLS-13 monomer concentration of <100 µM. The concentration of ngCA-R5 was  
517 adjusted to be no more than one-fifth of the AaLS-13 monomer concentration. The final NaCl concentration  
518 in the mixture was approximately 200 mM. This mixture was incubated at room temperature overnight to  
519 allow for the encapsulation of ngCA-R5 within AaLS-13 nanocages.

520

521      *pNPA Colorimetric Assay for Measuring CA Activity*

522           CA catalyzes the hydrolysis of pNPA, producing p-nitrophenol, a yellow product with strong  
523 absorbance at 405 nm. The assay was conducted in a 2 mL cuvette by preparing a reaction mixture  
524 consisting of 400 µL 0.1 mM pNPA in 50 mM, pH 7.4 Tris buffer, and 10 µL AaLS-13-encapsulated ngCA-  
525 R5. The absorbance of the reaction mixture at 405 nm was recorded every 30 seconds over a 3-minute  
526 period using a NanoDrop One<sup>C</sup> UV/Vis spectrophotometer (Thermo Scientific).

527

528      *CO<sub>2</sub> Mineralization with CA-LS Bionanoreactors*

529       The CA-LS bionanoreactors were mixed with MgCl<sub>2</sub> solution and CO<sub>2</sub>-saturated water in a 1.5 mL  
530   tube. CO<sub>2</sub>-saturated water was prepared by passing DI water through a 0.22 µm filter, cooling it in an ice-  
531   water slurry, and bubbling CO<sub>2</sub> gas at a flow rate of 0.5 mL/min for 30 min. The final solution contained 1  
532   mM Mg<sup>2+</sup> and 5.6 mM CO<sub>2</sub>, which was then incubated with CA-LS (CA enzyme activity of 1 Wilbur-  
533   Anderson unit/mL measured by the phenol red assay and 2 mg/mL of AaLS-13) at room temperature  
534   overnight to allow the precipitate to form.<sup>[66]</sup> Unencapsulated CA/LS and LS only controls were prepared  
535   using the same CA activity and AaLS-13 concentration. The final volume of the mixture was 1.4 mL. After  
536   thorough vortexing, 200 µL samples were taken, centrifuged at 12,000 × g three times to remove the  
537   supernatant, and the remaining pellets were dissolved in an acidic buffer (50 mM HEPES + 1% nitric acid)  
538   for Mg<sup>2+</sup> quantification using ICP-OES.

539

#### 540   *XRD Characterization*

541       The pellet formed by incubating Mg<sup>2+</sup> and CO<sub>2</sub> with CA-LS was collected and dried in a desiccator  
542   at room temperature. XRD data were obtained using a Bruker X-ray Diffraction System at the Nanoscale  
543   Fabrication and Characterization Facility (NFCF) at the University of Pittsburgh. Scans were conducted  
544   over a 2θ range of 10° to 95°, with a step size of 0.05° and a counting time of 2 seconds per step. The  
545   resulting diffraction patterns were analyzed using DIFFRAC.EVA to identify the peaks present and  
546   compare them with reference diffraction data.

547

#### 548   *Direct Air Capture*

549       The ability of CA-LS bionanoreactors to capture and mineralize CO<sub>2</sub> directly from the air was  
550   assessed using CA-LS bionanoreactors, assembled AaLS-13 nanocages, and purified ngCA-R5 in 50 mM  
551   HEPES buffer (pH 8.0) containing 40 mM MgCl<sub>2</sub> with the final concentrations of 0.75 mg/mL AaLS-13  
552   and/or 64.7 WAU/mL ngCA-R5. The mixtures were placed in 4 mL glass vials with loose caps and  
553   incubated at room temperature for 48 hours. To monitor the MgCO<sub>3</sub> precipitation over time, 800 µL samples  
554   were taken at various time intervals, and each sample was centrifuged at 12,000 × g three times to remove

555 the supernatant. The resulting pellets were dissolved in an acidic buffer and analyzed by ICP-OES for  
556 magnesium quantification.

557

558 **Supporting Information**

559 Supporting Information is available from the Wiley Online Library or from the author.

560

561 **Acknowledgments**

562 This work was supported by Pitt Momentum Funds, Pitt SSOE-SPH Pilot Grant, and the  
563 Department of Civil and Environmental Engineering at the University of Pittsburgh. Table of Contents, and  
564 Figures 2 and 5 were created with Biorender.com.

565

566 **Conflict of Interest**

567 The authors declare no conflict of interest.

568

569 **Data Availability Statement**

570 The data that support the findings of this study are available from the corresponding author upon  
571 reasonable request.

572 **References**

- 573 1. Smit, B.; Reimer, J. A.; Oldenburg, C. M.; Bourg, I. C., *Introduction to carbon capture and*  
574 *sequestration*. World Scientific: 2014; Vol. 1.
- 575 2. Ma, Y.; Yi, S.; Wang, M., *Carbon Capture Science & Technology* 2024, 13, 100257.
- 576 3. Romanov, V.; Soong, Y.; Carney, C.; Rush, G. E.; Nielsen, B.; O'Connor, W., *ChemBioEng Reviews*  
577 2015, 2 (4), 231-256.
- 578 4. Hills, C. D.; Tripathi, N.; Carey, P. J., *Frontiers in Energy Research* 2020, 8, 142.
- 579 5. Assen, A. H. A.; Belmabkhout, Y.; Adil, K.; Lachehab, A.; Hicham, H.; Hassoune, H.; Hicham, H.;  
580 Himanshu, A.; Himanshu, A.; Aggarwal, H., *Chemical Engineering Journal* 2021, 419, 129569. DOI  
581 10.1016/j.cej.2021.129569.
- 582 6. Azdarpour, A.; Guo, W.; Mohammad, A.; Asadullah, M.; Mohammad, A.; Junin, R.; Manan, M. A.;  
583 Hamidi, H.; Daud, A. R. M., *Energy Procedia* 2014, 61, 2783-2786. DOI  
584 10.1016/j.egypro.2014.12.311.
- 585 7. Pérez-López, R.; Montes-Hernandez, G.; Nieto, J. M.; Renard, F.; Charlet, L., *Applied Geochemistry*  
586 2008, 23 (8), 2292-2300.
- 587 8. Zhu, B.; Wilson, S.; Zeyen, N.; Raudsepp, M. J.; Zolfaghari, A.; Wang, B.; Rostron, B. J.; Snihur, K.  
588 N.; von Gunten, K.; Harrison, A. L., *Applied Geochemistry* 2022, 142, 105345.
- 589 9. McClendon, J. H., *Journal of Molecular Evolution* 1976, 8, 175-195.
- 590 10. Adams, E. E.; Caldeira, K., *Elements* 2008, 4 (5), 319-324.
- 591 11. Okyay, T. O.; Nguyen, H. N.; Castro, S. L.; Rodrigues, D. F., *Science of the Total Environment* 2016,  
592 572, 671-680.
- 593 12. Nanda, S.; Reddy, S. N.; Mitra, S. K.; Kozinski, J. A., *Energy Science & Engineering* 2016, 4 (2), 99-  
594 122.
- 595 13. Wang, J.; Watanabe, N.; Inomoto, K.; Kamitakahara, M.; Nakamura, K.; Komai, T.; Tsuchiya, N.,  
596 *Journal of Environmental Chemical Engineering* 2022, 10 (1), 107055.

- 597 14. García, S.; Liu, Q.; Maroto-Valer, M. M., *Greenhouse Gases: Science and Technology* **2014**, *4* (4), 544-  
598 554.
- 599 15. Gibbins, J.; Chalmers, H., *Energy policy* **2008**, *36* (12), 4317-4322.
- 600 16. Power, I. M.; Harrison, A. L.; Dipple, G. M.; Wilson, S.; Kelemen, P. B.; Hitch, M.; Southam, G.,  
601 *Reviews in Mineralogy and Geochemistry* **2013**, *77* (1), 305-360.
- 602 17. Chen, Y.; Feng, Y.; John Gregory, D.; Deveaux, J. G.; Masoud, M. A.; Felix Sunata, C.; Chandra, F. S.;  
603 Chen, H.; Huawei, C.; Zhang, D.; Lin, F.; Feng, L.; Lin, F., *Minerals* **2019**, *9* (2), 68. DOI  
604 10.3390/min9020068.
- 605 18. Kawahata, H.; Fujita, K.; Iguchi, A.; Inoue, M.; Iwasaki, S.; Kuroyanagi, A.; Maeda, A.; Manaka, T.;  
606 Moriya, K.; Takagi, H., *Progress in Earth and Planetary Science* **2019**, *6*, 1-37.
- 607 19. Wollast, R., *Bull Inst. Ocean Monaco Spec* **1994**, *13*, 13-35.
- 608 20. Zhang, X.; van Eldik, R.; Koike, T.; Kimura, E., *Inorganic Chemistry* **1993**, *32* (25), 5749-5755. DOI  
609 10.1021/ic00077a017.
- 610 21. de Oliveira Maciel, A.; Christakopoulos, P.; Rova, U.; Antonopoulou, I., *Chemosphere* **2022**, *299*,  
611 134419.
- 612 22. Baird, T. T.; Waheed, A.; Okuyama, T.; Sly, W. S.; Fierke, C. A., *Biochemistry* **1997**, *36* (9), 2669-2678.
- 613 23. Berland, S.; Marie, A.; Marie, A.; Denis, D.; Duplat, D.; Milet, C.; Sire, J. Y.; Bédouet, L.,  
614 *ChemBioChem* **2011**, *12* (6), 950-961. DOI 10.1002/cbic.201000667.
- 615 24. Arias, J. L.; Fernández, M. S., *Chemical Reviews* **2008**, *108* (11), 4475-4482. DOI 10.1021/cr078269p.
- 616 25. Chaves Filho, G. P.; Lima, M. E. G. B.; de Oliveira Rocha, H. A.; Moreira, S. M. G., *Carbohydrate  
617 Polymers* **2022**, *284*, 119204.
- 618 26. Mörtl, S.; Fischer, M.; Richter, G.; Tack, J.; Weinkauf, S.; Bacher, A., *Journal of Biological Chemistry*  
619 **1996**, *271* (52), 33201-33207.
- 620 27. Eita, S.; Donald, H., **2016**.
- 621 28. Wörsdörfer, B.; Woycechowsky, K. J.; Hilvert, D., *Science* **2011**, *331* (6017), 589-592.
- 622 29. Azuma, Y.; Hilvert, D., *Protein Scaffolds: Design, Synthesis, and Applications* **2018**, 39-55.

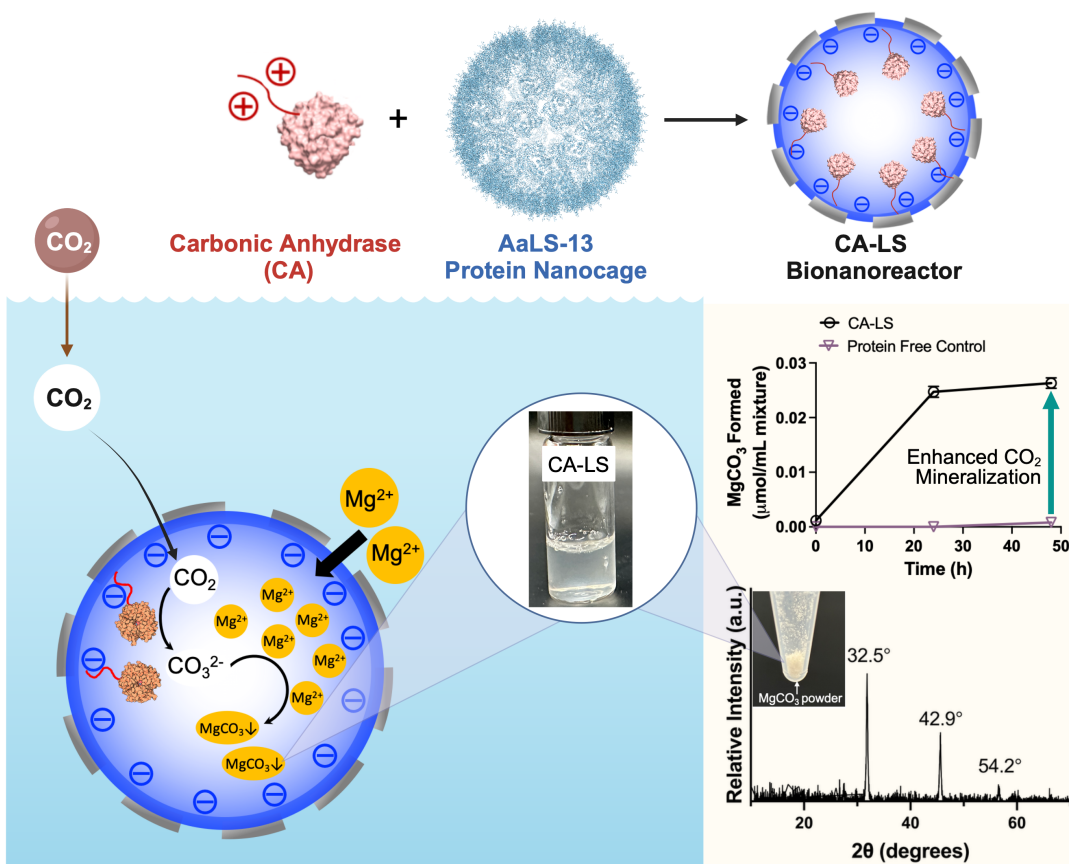
- 623 30. Azuma, Y.; Edwardson, T. G. W.; Hilvert, D., *Chemical Society Reviews* **2018**, 47 (10), 3543-3557.
- 624 31. Sasaki, E.; Böhringer, D.; Van De Waterbeemd, M.; Leibundgut, M.; Zschoche, R.; Heck, A. J. R.; Ban,  
625 N.; Hilvert, D., *Nature communications* **2017**, 8 (1), 14663.
- 626 32. Frey, R.; Mantri, S.; Rocca, M.; Hilvert, D., *Journal of the American Chemical Society* **2016**, 138 (32),  
627 10072-10075.
- 628 33. Azuma, Y.; Bader, D. L. V.; Hilvert, D., *Journal of the American Chemical Society* **2018**, 140 (3), 860-  
629 863.
- 630 34. Azuma, Y.; Zschoche, R.; Tinzl, M.; Hilvert, D., *Angewandte Chemie International Edition* **2016**, 55  
631 (4), 1531-1534.
- 632 35. Kaster, M. A.; Levasseur, M. D.; Edwardson, T. G. W.; Caldwell, M. A.; Hofmann, D.; Licciardi, G.;  
633 Parigi, G.; Luchinat, C.; Hilvert, D.; Meade, T. J., *ACS Applied Bio Materials* **2023**, 6 (2), 591-602.
- 634 36. Edwardson, T. G. W.; Levasseur, M. D.; Tetter, S.; Steinauer, A.; Hori, M.; Hilvert, D., *Chemical  
635 Reviews* **2022**, 122 (9), 9145-9197.
- 636 37. Tang, T. M. S.; Luk, L. Y. P., *Faraday Discussions* **2024**.
- 637 38. Frey, R.; Hayashi, T.; Hilvert, D., *Chemical Communications* **2016**, 52 (68), 10423-10426.
- 638 39. Azuma, Y.; Herger, M.; Hilvert, D., *Journal of the American Chemical Society* **2018**, 140 (2), 558-561.
- 639 40. Hänchen, M.; Prigobbe, V.; Baciocchi, R.; Mazzotti, M., *Chemical Engineering Science* **2008**, 63 (4),  
640 1012-1028.
- 641 41. Pead, S.; Durrant, E.; Webb, B.; Larsen, C.; Heaton, D.; Johnson, J.; Watt, G. D., *Journal of Inorganic  
642 Biochemistry* **1995**, 59 (1), 15-27. DOI [https://doi.org/10.1016/0162-0134\(94\)00050-K](https://doi.org/10.1016/0162-0134(94)00050-K).
- 643 42. Price, D. J.; Joshi, J. G., *Journal of Biological Chemistry* **1983**, 258 (18), 10873-10880.
- 644 43. Bade, M. M.; Dubale, A. A.; Bebizuh, D. F.; Atlabachew, M., *ACS omega* **2022**, 7 (22), 18770-18779.
- 645 44. Hailu, Y.; Tilahun, E.; Brhane, A.; Resky, H.; Sahu, O., *Groundwater for Sustainable Development*  
646 **2019**, 8, 457-467. DOI <https://doi.org/10.1016/j.gsd.2019.01.009>.
- 647 45. Guo, S.; Dan, Z.; Duan, N.; Chen, G.; Gao, W.; Zhao, W., *Environmental Science and Pollution  
648 Research* **2018**, 25, 30938-30948.

- 649 46. Hou, R.; Willumeit-Römer, R.; Garamus, V. M.; Frant, M.; Koll, J.; Feyerabend, F., *ACS applied*  
650 *materials & interfaces* **2018**, *10* (49), 42175-42185.
- 651 47. Seyrek, E.; Dubin, P. L.; Tribet, C.; Gamble, E. A., *Biomacromolecules* **2003**, *4* (2), 273-282.
- 652 48. Zhang, F.; Skoda, M. W. A.; Jacobs, R. M. J.; Martin, R. A.; Martin, C. M.; Schreiber, F., *The Journal*  
653 *of Physical Chemistry B* **2007**, *111* (1), 251-259.
- 654 49. Zhou, H.-X.; Pang, X., *Chemical reviews* **2018**, *118* (4), 1691-1741.
- 655 50. Sheinerman, F. B.; Honig, B., *Journal of molecular biology* **2002**, *318* (1), 161-177.
- 656 51. Jo, B. H.; Seo, J. H.; Yang, Y. J.; Baek, K.; Choi, Y. S.; Pack, S. P.; Oh, S. H.; Cha, H. J., *Acs Catalysis*  
657 **2014**, *4* (12), 4332-4340.
- 658 52. Koziej, L.; Gawin, A.; Azuma, Y., Lumazine synthase nanocompartments. In *Microbial Production of*  
659 *High-Value Products*, Springer: 2022; pp 335-355.
- 660 53. Nam, D. H.; Lee, J.-O.; Sang, B.-I.; Won, K.; Kim, Y. H., *Applied biochemistry and biotechnology*  
661 **2013**, *170*, 25-31.
- 662 54. Chirică, L. C.; Elleby, B.; Jonsson, B. H.; Lindskog, S., *European journal of biochemistry* **1997**, *244*  
663 (3), 755-760.
- 664 55. Anderson, J.; Byrne, T.; Woelfel, K. J.; Meany, J. E.; Spyridis, G. T.; Pocker, Y., *Journal of chemical*  
665 *education* **1994**, *71* (8), 715.
- 666 56. De Silva, P.; Bucea, L.; Sirivivatnanon, V., *Cement and concrete research* **2009**, *39* (5), 460-465.
- 667 57. Gadikota, G.; Swanson, E. J.; Zhao, H.; Park, A.-H. A., *Industrial & Engineering Chemistry Research*  
668 **2014**, *53* (16), 6664-6676.
- 669 58. Yuen, Y. T.; Sharratt, P. N.; Jie, B., *Environmental Science and Pollution Research* **2016**, *23*, 22309-  
670 22330.
- 671 59. Breyer, C.; Fasihi, M.; Bajamundi, C.; Creutzig, F., *Joule* **2019**, *3* (9), 2053-2057.
- 672 60. Sovacool, B. K.; Baum, C. M.; Low, S.; Roberts, C.; Steinhauser, J., *Environmental Research Letters*  
673 **2022**, *17* (7), 074014.
- 674 61. Razowska-Jaworek, L., *Calcium and Magnesium in Groundwater*. CRC Press: **2014**.

- 675 62. Zhu, Y.; Li, W.; Sun, G.; Tang, Q.; Bian, H., *International Journal of Greenhouse Gas Control* **2016**,  
676 49, 290-296.
- 677 63. Migliardini, F.; De Luca, V.; Carginale, V.; Rossi, M.; Corbo, P.; Supuran, C. T.; Capasso, C., *Journal*  
678 *of Enzyme Inhibition and Medicinal Chemistry* **2014**, 29 (1), 146-150.
- 679 64. Cheng, L.; Zhang, L.; Chen, H.; Gao, C., *Separation and purification technology* **2006**, 50 (3), 324-  
680 329.
- 681 65. Zhou, C.; Ni, J.; Chen, H.; Guan, X., *Sustainable Energy & Fuels* **2021**, 5 (17), 4355-4367.
- 682 66. Wilbur, K. M.; Anderson, N. G., *The Biological Bulletin* **1950**, 98 (1), 19-24.

683 **Table of Contents**

684 This study introduces a bionanoreactor approach for sustainable carbon capture and sequestration  
 685 (CCS) using self-assembling AaLS-13 protein nanocages. Encapsulating carbonic anhydrase, these  
 686 nanocages concentrate metal cations to facilitate CO<sub>2</sub> mineralization under benign, ambient conditions,  
 687 efficiently converting both dissolved and atmospheric CO<sub>2</sub> into stable carbonate minerals. The findings  
 688 highlight AaLS-13-based bionanoreactors as a sustainable CCS alternative and provide new insights for  
 689 leveraging AaLS-13-substrate interactions to enhance enzyme catalysis in diverse future applications.



690

1                   **SUPPORTING INFORMATION**

2

3                   **Protein-Based Enzyme Bionanoreactor for Efficient**  
4                   **CO<sub>2</sub> Mineralization under Benign Conditions**

5

6                   Yifei Ma<sup>a</sup>, Meng Wang<sup>a,\*</sup>

7

8                   <sup>a</sup>Department of Civil and Environmental Engineering, University of Pittsburgh, 3700 O'Hara St.,  
9                   Pittsburgh, PA 15261, USA

10                  \*Address correspondence to [meng.wang@pitt.edu](mailto:meng.wang@pitt.edu), 412-624-9207

11

12 **EXPERIMENTAL METHODS**

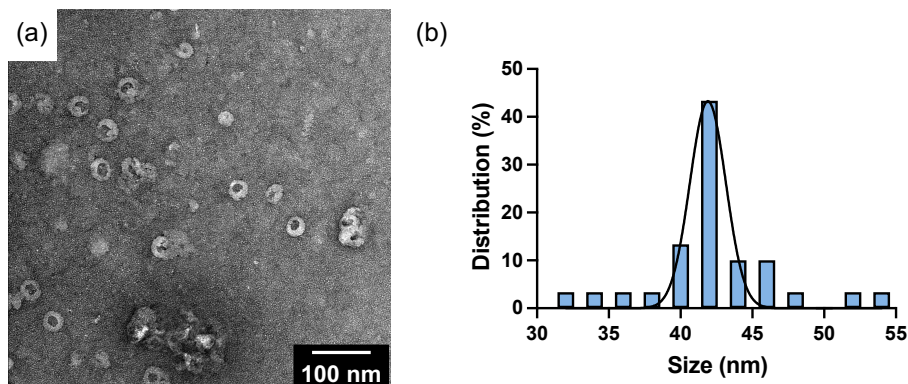
13 **Phenol Red CO<sub>2</sub> Hydration Activity Assay**

14 CO<sub>2</sub>-saturated water was prepared by bubbling CO<sub>2</sub> gas through ice-cold deionized water at a flow  
15 rate of 1 L/min for 30 minutes, achieving a saturation concentration of approximately 40 mM. This saturated  
16 solution was then diluted with ice water to obtain final CO<sub>2</sub> concentrations of 10 mM. A 100 µM phenol  
17 red solution was prepared in a 20 mM HEPES buffer at pH 8.3. The reaction mixture, consisting of 200 µL  
18 of the phenol red solution, 10 µL of purified CA-LS, and 200 µL of 10 mM CO<sub>2</sub> solution, was rapidly mixed  
19 in a 2 mL cuvette. The cuvette was then immediately put in a Thermo Scientific Nanodrop One<sup>C</sup>  
20 Spectrophotometer, and the absorbance at 560 nm was continuously monitored at 2-second intervals. The  
21 color change from orange to yellow in the phenol red solution indicates a shift from a slightly alkaline or  
22 neutral pH towards a more acidic environment, as CA catalyzes the conversion of CO<sub>2</sub> and water into  
23 bicarbonate and protons (H<sup>+</sup>). The increased concentration of H<sup>+</sup> lowers the pH, leading to the protonation  
24 of phenol red and the associated color shift.

25 **FIGURES AND TABLE**

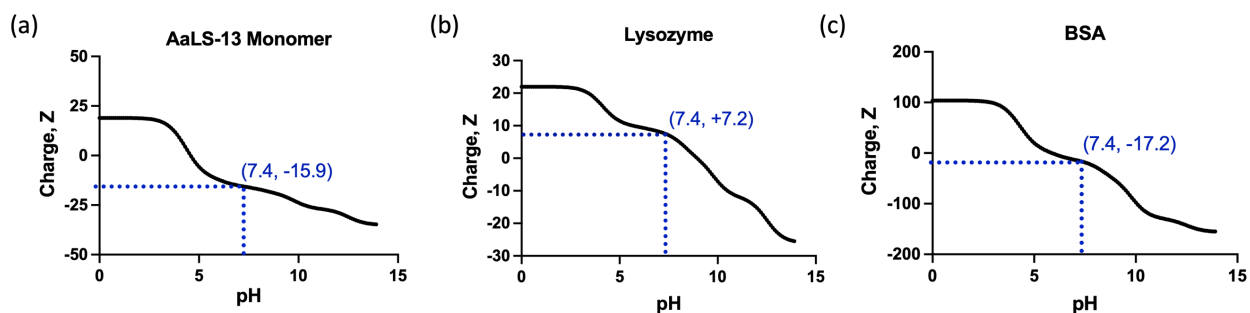
26

27



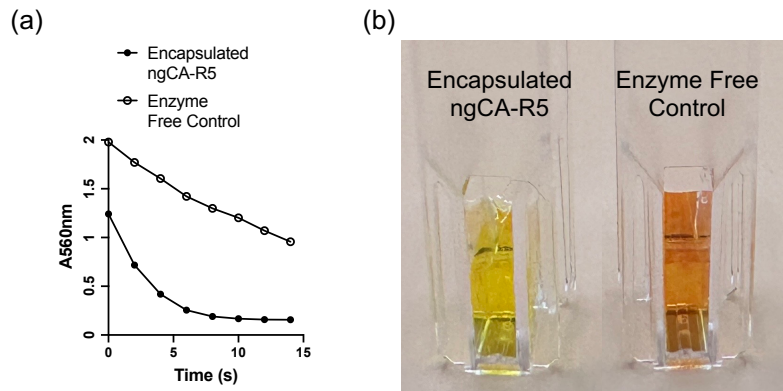
28 **Figure S1.** (a) Negative-stain TEM image of assembled AaLS-13 protein nanocages (5  $\mu$ M monomer  
29 concentration). The stained proteins appear as bright circles against the dark background. (b) Particle size  
30 distribution curve derived from TEM images, indicating that the majority of AaLS-13 protein nanocage  
31 diameters cluster around 42.5 nm.

32



33 **Figure S2.** Titration curves of AaLS-13 monomer (a), lysozyme (b), and BSA (c). The overall protein  
34 charges at pH 7.4 are -15.9, +7.2, and -17.2 for AaLS-13, lysozyme, and BSA, respectively.

35



36 **Figure S3.** (a) Spectrophotometric data from phenol red assays measuring CO<sub>2</sub> hydration activity of CA-  
37 LS bionanoreactors. Absorbance at 560 nm was recorded every 2 seconds for a total of 14 seconds. The  
38 enzyme free control group was performed under the same experimental conditions for comparison. The  
39 absorbance of the CA-LS added group demonstrated a more rapid and steep decline as compared to the  
40 enzyme free control group. (b) Pictures illustrating the solution color difference between the encapsulated  
41 ngCA-R5 within AaLS-13 nanocage and enzyme free groups. The CA-LS added group appeared yellow  
42 due to a decrease in pH, while the enzyme-free control remained orange.

43 **Table 1.** Primer and protein encoding sequences used in this study. The yellow DNA sequence refers to  
 44 ngCA, red refers to R5, blue refers to AaLS-13, and green refers to 6×His tag.

<b>R5-F</b>	GTCCAAAGGTAGCAAGCGCCGTATCCTGAAGCTTCATCACCATCACCATCATT AAGGATC
<b>R5-R</b>	CCAGAATAACTTCCGGACTTTGCTTGAAAGCTTTCAATCACCAACGCGCGC
<b>ngCA- R5-6His- pET21b+</b>	ATG <b>CATGGCAACCATA</b> CCCATTGGGGCTATACCGGCCATGATA <b>GCCCCGAA</b> <b>GCTGGGGCAACCTGAGCGAAGA</b> ATTTCGCCTGTGCAGCACCGGAAAAATCA GAGCCC <b>GGTGAACATTACCGAAACCGTGAGCGGCAA</b> ACTGCCGGCGATTAAA GTGA <b>ACTATAAACCGAGCATGGTGGATGTGGAAAACA</b> ACGGCCATACCATT AAGTGA <b>ACTATCCGGAAGGC</b> GGCAACACCCCTGACCGTGAA <b>CGGCCG</b> CACCTA TACCC <b>TGAAACAGTT</b> CATTTCATGTGCCGAGCGAAA <b>ATCAGATTAAGGCC</b> GCAC <b>CTTCCGATGGAAGCGC</b> ATTGTGCATCTGGATGAAA <b>ACAAACAGCCG</b> CTGGTG <b>CTGGCGGTGCTGTATGAAAGCGGGAAA</b> CCAACGCCGCGCTGAGCA GCATTGGA <b>ACGTGATGCCGATGACCGCGGCAA</b> AGTGA <b>AACTGAATCAGCC</b> GTTTG <b>ATGCGAGCACCC</b> TGCTGCCGAA <b>ACGCCTGAA</b> ATATTATCGCTTGCG GCAGC <b>CTGACCACCCGCCGTGCACCGAAGGCGTGAGCTGGCTGGTGTGAA</b> AAC <b>CTATGATCATATTGATCAAGCGCAAGCGGAAA</b> ATTACCCGCGCGTG GGCAGCGAAA <b>ACAACCGCCCGTGAGCCGCTGAA</b> CGCGCGCTGGTATTG <b>AAAAGCTTCAGCAAGCAAAAGTCCGGAAGTTATTCTGGGTCAAAGGTAGCAA</b> <b>GCGCGTATCCTG</b> CATCATCATCATCAT <b>TAA</b>
<b>AaLS-13- 6His- pET28b+</b>	ATG <b>GGAAATTATGAAAGGCAA</b> ACTGACCGCGGAAGGCCTGCGCTTGGCATTG TGGCGAGCCGCTTAACC <b>ATGCGCTGGTGGCCGCGAAGAAGA</b> AGATATTACCC <b>CTGGTGTGCG</b> TGATTGCATTGTGCGTCATGGCGGCCGCGAAGAAGA <b>AGATATTACCC</b> CTGGTGTGCG TGCGGGCAGCTGGAAATTCCGGTGGCGCGGGCGA <b>ACTGGCGCGCAAAGA</b> AGATATTGATGCGGTATTGCGATTGGCG <b>CTGATTGAAAGGCGCGAACCG</b> CATTGATTATATTGCGAGCGA <b>AGTGAGCAAAGGCTGGCGAACCTGAGCCT</b> GGA <b>ACTGCGCAAACCGATTAGCTTGGCGATATTACCGATGATGAA</b> CTGGAA GAAGCGATTGA <b>ATGCGCGGGCACCGAACATGGCAACAAAGGCTGGGAAGCG</b> GCG <b>CTGAGCGCGATTGAAATGGCGAACCTGTTAAAAGCCTGCGCCTGGAAAC</b> ATCATCATCATCAT <b>TAA</b>

45